

The acceleration of cosmic-ray protons in the supernova remnant RX J1713.7–3946

R. Enomoto*, T. Tanimori†, T. Naito‡, T. Yoshida§, S. Yanagita§, M. Mori*, P. G. Edwards||, A. Asahara†, G. V. Bicknell¶, S. Gunji#, S. Hara☆☆, T. Hara‡, S. Hayashi**, C. Itoh§, S. Kabuki*, F. Kajino**, H. Katagiri*, J. Kataoka†, A. Kawachi*, T. Kifune††, H. Kubo†, J. Kushida☆☆, S. Maeda**, A. Maeshiro**, Y. Matsubara‡‡, Y. Mizumoto§§, M. Moriya☆☆, H. Muraishi|||, Y. Muraki‡‡, T. Nakase¶¶, K. Nishijima¶¶, M. Ohishi*, K. Okumura*, J. R. Patterson##, K. Sakurazawa☆☆, R. Suzuki*, D. L. Swaby##, K. Takano☆☆, T. Takano#, F. Tokana||, K. Tsuchiya*, H. Tsunoo*, K. Uruma¶¶, A. Watanabe# & T. Yoshikoshi☆☆

* Institute for Cosmic Ray Research, University of Tokyo, Kashiwa, Chiba 277-8582, Japan
 † Department of Physics, Kyoto University, Sakyo-ku, Kyoto 606-8502, Japan
 ‡ Faculty of Management Information, Yamanashi Gakuin University, Kofu, Yamanashi 400-8575, Japan
 § Faculty of Science, Ibaraki University, Mito, Ibaraki 310-8512, Japan
 || Institute of Space and Astronautical Science, Sagami-hara, Kanagawa 229-8510, Japan
 ¶ Mt Stromlo and Siding Spring Observatories, Australian National University, ACT 2611, Australia
 # Department of Physics, Yamagata University, Yamagata, Yamagata 900-8560, Japan
 ☆ Department of Physics, Tokyo Institute of Technology, Meguro-ku, Tokyo 152-8551, Japan
 ** Department of Physics, Konan University, Kobe, Hyogo 658-8501, Japan
 †† Faculty of Engineering, Shinshu University, Nagano, Nagano 380-8553, Japan
 ‡‡ Solar-Terrestrial Environment Laboratory, Nagoya University, Nagoya, Aichi 464-8601, Japan
 §§ National Astronomical Observatory of Japan, Mitaka, Tokyo 181-8588, Japan
 ||| Ibaraki Prefectural University of Health Sciences, Ami, Ibaraki 300-0394, Japan
 ¶¶ Department of Physics, Tokai University, Hiratsuka, Kanagawa 259-1292, Japan
 ## Department of Physics and Mathematical Physics, University of Adelaide, SA 5005, Australia
 ☆☆ Department of Physics, Osaka City University, Osaka, Osaka 558-8585, Japan

Protons with energies up to $\sim 10^{15}$ eV are the main component¹ of cosmic rays, but evidence for the specific locations where they could have been accelerated to these energies has been lacking². Electrons are known to be accelerated to cosmic-ray energies in supernova remnants^{3,4}, and the shock waves associated with such remnants, when they hit the surrounding interstellar medium, could also provide the energy to accelerate protons. The signature of such a process would be the decay of pions (π^0), which are generated when the protons collide with atoms and molecules in an interstellar cloud: pion decay results in γ -rays with a particular spectral-energy distribution^{5,6}. Here we report the observation of cascade showers of optical photons resulting from γ -rays at energies of $\sim 10^{12}$ eV hitting Earth's upper atmosphere, in the direction of the supernova remnant RX J1713.7–3946. The spectrum is a good match to that predicted by pion decay, and cannot be explained by other mechanisms.

RX J1713.7–3946 is a shell-type supernova remnant (SNR) that was found in the ROSAT all-sky survey⁷. Observations with the ASCA satellite have revealed intense non-thermal X-ray emission from the northwest rim⁸, and TeV γ -ray emission ($1 \text{ TeV} = 10^{12} \text{ eV}$) has been detected from the northwest rim by the CANGAROO ('collaboration of Australia and Nippon for a γ -ray observatory in the outback') 3.8-m Cerenkov telescope⁹. Infrared and radio observations have revealed the possible association of the SNR with a

molecular cloud complex¹⁰.

The CANGAROO air Cerenkov telescope, which is intended to detect very high energy γ -rays, is located near Woomera, South Australia. The 3.8-m telescope⁹, which operated from 1994 to 1998, was replaced in 2000 by a 10-m reflector with a 552-pixel camera of 0.115° square photomultiplier pixels. Observations of RX J1713.7–3946 were carried out 23–26 July and 19–27 August 2000, and 20 May–26 June 2001 with the 10-m telescope. After selecting data taken at high elevation angles ($>60^\circ$) in good weather conditions, a total of 2,332 min on-source and 1,789 min off-source data remained for further analysis.

The differential fluxes of γ -rays from RX J1713.7–3946 are plotted in Fig. 1. The number of excess events was determined from the plots of image orientation angle (α ; ref. 11) for on- and off-source runs (Fig. 1 inset) to be $3,417 \pm 240$ (14.3σ). The best fit of

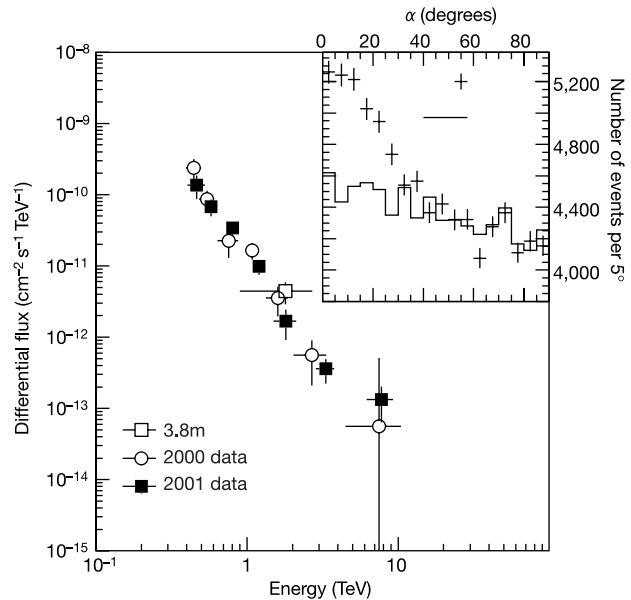


Figure 1 Differential fluxes, and distributions of the image orientation angle α (inset). Main figure: data shown by open circles and filled squares were obtained in this experiment, the open square shows data from CANGAROO-I (3.8 m)⁹. The CANGAROO-I integral flux was multiplied by 1.5 and divided by energy (TeV), assuming that the energy spectrum is proportional to $E^{-2.5}$. Inset, points with error bars show the distribution of α for on-source data, and that for off-source is shown by the histogram. These were obtained as follows: first, 'cleaning' cuts on camera images were applied, requiring pixel pulse-heights of greater than ~ 3.3 photoelectrons, Cerenkov photon arrival times within 40 ns, and clusters of at least five adjacent triggered pixels in each event. The conventional imaging parameters¹¹ were then calculated. After applying an energy dependent distance cut, we used the shape parameters to calculate likelihoods (L ; ref. 26) under the assumptions of both γ -ray and proton origins for the cascade. The final on- and off-source data sets were obtained by excluding events with a likelihood ratio $L(\gamma - ray) / [L(\gamma - ray) + L(\text{proton})] < 0.4$ (ref. 27). The number of excess events was determined from the plots of image orientation angle α for on- and off-source runs (inset) to be $3,417 \pm 240$ (14.3σ). The γ -ray acceptance efficiency was calculated using the Monte Carlo method²⁶. In order to check our simulations, we analysed Crab nebula data obtained in December 1999 and December 2000, and found that the flux was consistent with previous experiments²⁸ to within 12%. In addition, we checked the cosmic-ray spectrum between 100 GeV and 30 TeV. The effects of night-sky background, trigger, and electronics saturation were estimated and included in uncertainties. The systematic uncertainty due to likelihood, clustering methods and pixel triggering threshold was estimated to be 20%. The energy scale uncertainty from the mirror reflectivity, mirror segment distortions, and Mie scatterings was calculated to be 15% (point to point) and 20% (overall).

the 10-m telescope results gives:

$$dF/dE = (1.63 \pm 0.15 \pm 0.32) \times 10^{-11} E^{-2.84 \pm 0.15 \pm 0.20} \quad (1)$$

where the first errors are statistical and the second are systematic with a χ^2/DOF (number degree of freedom) of 0.97, and dF/dE is in units of $\text{cm}^{-2} \text{s}^{-1} \text{TeV}^{-1}$. F and E are the gamma-ray flux and energy, respectively. When the results were fitted with a spectrum with an energy cut-off such as $\propto E^{-2} e^{-E/E_{\text{max}}}$, an E_{max} of $3.3 \pm 0.7 \text{ TeV}$ was obtained with $\chi^2/\text{DOF} = 2.3$. The fluxes are also shown in Fig. 2, multiplied by E^2 , together with multiwavelength spectra and theoretical predictions (described below). RX J1713.7–3946 is one of the intrinsically brightest galactic TeV γ -ray sources discovered, and it is notable that the power-law spectrum increases monotonically as energy decreases. This is in contrast to the spectrum of SN1006, which flattens below 1 TeV (ref. 12), consistent with synchrotron/inverse Compton (IC) models^{13–16}. Both SNRs emit X-rays via the synchrotron process, but the differing TeV spectra suggest a different emission mechanism should be acting in RX J1713.7–3946 at TeV energies.

The morphology of the TeV γ -ray emitting region is shown by the thick solid contours in Fig. 3, together with the ASCA $>2\text{-keV}$ intensity contours¹⁷ and IRAS $100\text{-}\mu\text{m}$ results. The observed TeV γ -ray intensity peak coincides with the northwest rim, and the emission extends over the ASCA contours. A possible extension towards the CO cloud in the northeast¹⁸ can also be seen.

The broadband spectrum plotted in Fig. 2 was derived using data

from ATCA (Australia Telescope Compact Array)¹⁹, ASCA^{8,17}, the EGRET²⁰ satellite-borne telescope and this work. In order to explain this spectrum, we considered three mechanisms: the synchrotron/IC process, synchrotron/bremsstrahlung, and π^0 decay produced by proton–nucleon collisions. The momentum spectra of incident particles (electrons and protons) are assumed to be:

$$dN/cdp = N_0(p/mc)^{-\alpha} \exp(-p/p_{\text{max}}) \quad (2)$$

where dN/cdp is in units of $\text{cm}^{-3} \text{TeV}^{-1}$. N is the number of particles, N_0 is the normalization factor, p is the momentum of the particle, m is the mass of the particle, c is the velocity of light, p_{max} is the maximum momentum of accelerated particles, and α is the index of the power law spectrum. The effects of acceleration limits from the age and size of the SNR are included in the exponential term. Best-fit values for the radio and X-ray fluxes due to synchrotron radiation from electrons²¹ are 2.08 for α , 126 for $p_{\text{max}} c B^{0.5}$, and 2.00 for $N_0 (V/4\pi d^2) (B)^{(\alpha+1)/2}$; here V is the volume of the radiation region, d is the distance from the Earth, $p_{\text{max}} c$ is in units of TeV, and B is in units of μG . The acceptable ranges for these parameters are 1.99–2.13, 93–139 and 4.06–0.58 respectively. The resultant best fit is plotted in Fig. 2 as the solid line.

We initially assumed the 2.7 K cosmic microwave background as the seed photons for IC scattering, where the Klein–Nishina formula was used. A similar model, applied to SN1006, matched the multiband spectrum well^{15,16}. Here, the best-fit values derived for synchrotron radiation from the incident electrons were used, and we assumed that the synchrotron and IC emission regions were the

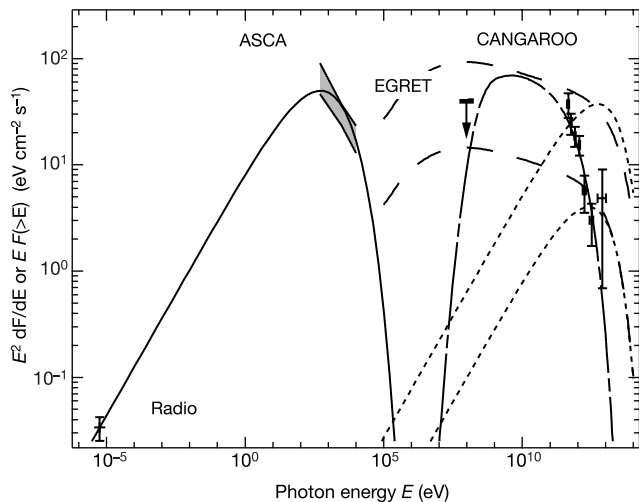


Figure 2 Multi-band emission from RX J1713.7–3946, and emission models. The radio observation was made with ATCA¹⁹. The ATCA flux at 1.36 GHz is estimated from two bright filaments lying in the northwest rim of RX J1713.7–3946 to be $S = 4 \pm 1 \text{ Jy}$ (ref. 19). The shaded area between the thick lines indicates the X-ray emission measured by the GIS detector on the ASCA satellite¹⁷. The integral flux between 0.5 and 10.0 keV was obtained from Table 4.5 in ref. 17 and the spectral index in Table 4.4. The differential flux was calculated from these two values at 3 keV, the mean GIS sensitivity. The flux uncertainty due to the extended structure of the source was considered to be within $+10\%/-30\%$, which was calculated following the procedure described in ref. 29. The EGRET upper limit corresponds to the flux of 3EG J1714–3857²⁰. The TeV γ -ray points are from this work (CANGAROO). Lines show model calculations: synchrotron emission (solid line), inverse Compton emission (dotted lines), bremsstrahlung (dashed lines) and emission from π^0 decay (short-long dashed line). Inverse Compton emission and bremsstrahlung are plotted for two cases: $3 \mu\text{G}$ (upper curves) and $10 \mu\text{G}$ (lower curves). The distance to this SNR has ambiguity as follows; the rotation velocity of the associated molecular cloud from this observation yielded a distance to the SNR of $6 \pm 1 \text{ kpc}$, in contrast to the distance of 1 kpc estimated from soft-X-ray absorption⁸. The age for the SNR is estimated to be more than 10,000 yr (for a distance of 6 kpc) or $\sim 2,000 \text{ yr}$ (for 1 kpc). Details of these models are given in the text.

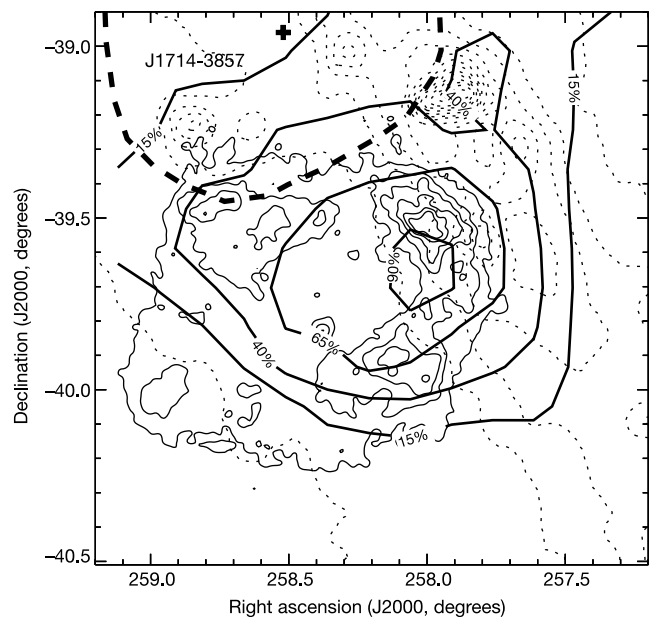


Figure 3 Profile of emission around the northwest rim of RX J1713.7–3946. The telescope tracked the point in the northwest rim of the SNR from which the maximum X-ray flux was detected (right ascension 257.9875° , declination -39.5311° in J2000 coordinates)⁸. The solid thick contours are obtained from our observations. These contours were calculated from the distribution of the detection significance determined at each location from the differences in the α plots (on- minus off-source histogram) divided by the statistical errors. The angular resolution was estimated to be 0.23° (1σ , 68% confidence level). There is a possible systematic offset of the order of 0.1° . The detection efficiency drops rapidly outside a 0.5° circle from the northwest rim, that is, the telescope pointing position. The solid thin contours are the ASCA data, and the dotted contours are IRAS $100\text{-}\mu\text{m}$ data. The sub-GeV source 3EG J1714–3857 is listed in the third EGRET catalogue²⁰ with a 95% confidence contour which includes the northeast rim (the thick dashed contour). 3EG J1714–3857 is marginally coincident with RX J1713.7–3946 and is an extended source, although there may be source confusion in this area²⁰.

same. Two representative magnetic field strengths, 3 and 10 μG , were used. The results, plotted with dotted lines in Fig. 2, show that these models are not consistent with the observed sub-TeV spectrum.

A clear feature of the synchrotron/IC process is the correlation between the peak flux and its energy. We carried out a further study of the above parameter space, taking into account the following uncertainties. For the incident-electron flux, the (1σ) fitting uncertainties were used, and we included IR emission for the IC seed photons. The IR background in the inner region of the Galaxy is not well known. We adopted a model²² that assumes a temperature of 40 K and an energy density incorporating a dilution factor. The maximum energy density was set to 1 eV cm^{-3} in order not to exceed the energy densities of cosmic rays or magnetic fields. For example, IR density at 20' apart from the nearby H II cloud (G347.61+0.20, which is the nearest and brightest IR source) was estimated to be 0.93 eV cm^{-3} using equation (3) in ref. 23. The IC calculation was carried out both with and without this IR maximum energy emission in the IC process, assuming the various incident-electron spectra. The shaded area on the right side of Fig. 4 is the resulting theoretically allowed region, with the experimentally allowed region shown by the shaded area on the left side of the figure. The predictions of synchrotron/IC models are inconsistent with our experimental data by an order of magnitude.

Although we have investigated simple cases, there is the possibility that the electron spectrum may soften at higher energies owing to synchrotron cooling. The cooling is severest in the case of the >10,000-year-old SNR for electrons exceeding E_{cool} , which is the critical energy estimated in comparison with the acceleration rate and cooling rate. If $E_{\text{cool}} < p_{\text{max}}c$, plateau-like features would

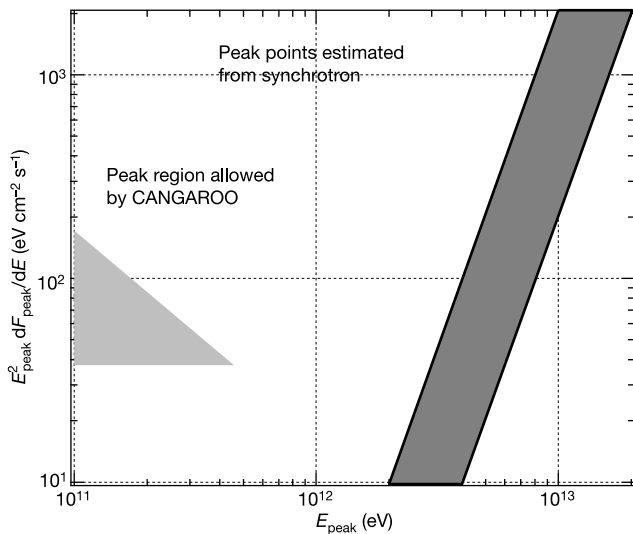


Figure 4 Allowed regions in the parameter space defined by peak flux ($E_{\text{peak}}^2 dF_{\text{peak}}/dE$) plotted against peak energy. The peak energies and fluxes for IC processes are allowed in this parameter space. The experimental flux (Fig. 2) shows the simple power-law spectrum between 400 GeV and 8 TeV, and hence the peak energy—if the IC-process is dominant—should be lower than the lowest-energy CANGAROO detection point. This corresponds to the lower-right corner of the shaded area on the left. The energy spectrum below the IC peak must flatten, and so by assuming a power-law spectral index of 2.84 for energies below 400 GeV, the experimentally allowed region is defined. On the other hand, theoretical estimates were carried out considering both the 2.7 K CMB alone, and a combination of the IR (40 K) background and the 2.7 K CMB, as target photon sources. The uncertainties from the synchrotron model fitting and those for IR (40 K) flux are taken into account. The shaded area on the right of the figure is the theoretically allowed region (1σ) under the assumption of IC process. As there is no overlap with the observationally allowed region, we can rule out IC models for the TeV γ -ray production.

appear in both the synchrotron and IC fluxes shown in Fig. 2, similar to the cases of pulsar nebulae²⁴ and blazars²⁵. These still would not fit our experimental results.

The bremsstrahlung spectrum was calculated assuming that it occurs in the same region as the synchrotron radiation. A material density of 300 protons cm^{-3} was assumed. The dashed lines in Fig. 2, for magnetic fields of 3 and 10 μG , are both inconsistent with our observation. In addition, the bremsstrahlung model is unable to simultaneously reproduce the observed GeV and TeV fluxes. Even if we neglect the EGRET data, a magnetic field of the order of 1 G with a material density of 17,500 protons cm^{-3} would be necessary. Both values are unreasonably high.

Thus electron-based models fail to explain the observational results, and so we examined π^0 decay models. The π^0 's are produced in collisions of accelerated protons with interstellar matter. A model⁶ adopting Δ -resonance and scaling was used. We adopted parameters for equation (2) of $\alpha = 2.08$ and $p_{\text{max}}c = 10$ TeV, considering the plausible parameter regions of typical shock acceleration theory. (If we simply assume the same cut-off energy for electrons, it follows from the best-fit value for the parameter $p_{\text{max}}cB^{0.5}$ of 126 that the magnetic field might be as large as 100 μG .) The result is shown by the short-long dashed curve in Fig. 2. The best-fit parameters for the total energy of accelerated protons E_0 and matter density n_0 must satisfy the equation $(E_0/10^{50})(n_0)(d/6)^{-2} = 300$; here d is the distance (in kpc) to RX J1713.7–3946, E_0 is in erg, n_0 is in protons cm^{-3} . A value of $E_0 \approx 10^{50}$ erg gives n_0 of the order of 10 or 100 protons cm^{-3} for distances of 1 or 6 kpc, respectively. Both cases are consistent with the molecular column density estimated from Fig. 7 of ref. 10. Assuming a larger value of p_{max} would allow the value of $(E_0/10^{50})(n_0)(d/6)^{-2}$ to be reduced. The π^0 model alone, therefore, readily explains our results, which provide observational evidence that protons are accelerated in SNRs to at least TeV energies. \square

Received 9 January; accepted 28 February 2002.

1. Simpson, J. A. Elemental and isotopic composition of the galactic cosmic-rays. *Annu. Rev. Nucl. Part. Sci.* **33**, 323–381 (1983).
2. Pohl, M. *Proc. 27th Int. Cosmic Ray Conf. (Hamburg) 2001, Rapporteur talk* (eds Simon, M., Lorenz, E. & Pohl, M.) (Copernicus Gesellschaft e.V., Katlenburg-Lindau, Germany, in the press); also as preprint astro-ph/0111552 at <http://xxx.lanl.gov> (2001).
3. Koyama, K. *et al.* Evidence for shock acceleration of high-energy electrons in the supernova remnant SN1006. *Nature* **378**, 255–258 (1995).
4. Tanimori, T. *et al.* Discovery of TeV gamma rays from SN 1006: Further evidence for the supernova remnant origin of cosmic rays. *Astrophys. J.* **497**, L25–L28 (1998).
5. Aharonian, F. A., Drury, L. O'C. & Völk, H. J. GeV/TeV gamma-ray emission from dense molecular clouds overtaken by supernova shells. *Astron. Astrophys.* **285**, 645–647 (1994).
6. Naito, T. & Takahara, F. High energy gamma-ray emission from supernova remnants. *J. Phys. G* **20**, 477–486 (1994).
7. Pfeffermann, E. & Aschenbach, B. in *Roentgenstrahlung from the Universe* (eds Zimmermann, H. H., Trümper, J. & Yorke, H.) 267–268 (MPE Report 263; Max-Planck-Institut fuer Extraterrestrische Physik, Garching, 1996).
8. Koyama, K. *et al.* Discovery of non-thermal X-rays from the northwest shell of the new SNR RX J1713.7–3946: The second SN 1006? *Publ. Astron. Soc. Jpn* **49**, L7–L11 (1997).
9. Muraishi, H. *et al.* Evidence for TeV gamma-ray emission from the shell type SNR RXJ1713.7–3946. *Astron. Astrophys.* **354**, L57–L61 (2000).
10. Slane, P. *et al.* Nonthermal X-ray emission from the shell-type supernova remnant G347.3–0.5. *Astrophys. J.* **525**, 357–367 (1999).
11. Hillas, A. M. in *Proc. 19th Int. Cosmic Ray Conf. (La Jolla) Vol. 3*, 445–448 (NASA Conference publication, 1985).
12. Tanimori, T. *et al.* in *Proc. 27th Int. Cosmic Ray Conf. (Hamburg)* (eds Simon, M., Lorenz, E. & Pohl, M.) Vol. 6, 2465–2468 (Copernicus Gesellschaft e.V., Katlenburg-Lindau, Germany, 2001).
13. Aharonian, F. A. & Atayan, A. M. On the origin of TeV radiation of SN 1006. *Astron. Astrophys.* **351**, 330–340 (1999).
14. Mastichiadis, A. & de Jager, O. C. TeV emission from SN 1006. *Astron. Astrophys.* **311**, L5–L8 (1996).
15. Yoshida, T. & Yanagita, S. *Proc. 2nd INTEGRAL Workshop 'The Transparent Universe'* 85–88 (ESA SP-382 European Space Agency, Noordwijk, Netherlands, 1997).
16. Naito, T., Yoshida, T., Mori, M. & Tanimori, T. Radio to TeV gamma-ray emission from SN 1006 and shock acceleration around its rim. *Astron. Nachr.* **320**, 205–206 (1999).
17. Tomida, H. *Synchrotron Emission from the Shell-like Supernova Remnants and the Cosmic-Ray Origin* Thesis, Kyoto Univ. (1999).
18. Butt, Y. M., Torres, D. F., Combi, J. A., Dame, T. & Romero, G. Is the supernova remnant RX J1713.7–3946 a hadronic cosmic ray accelerator? *Astrophys. J.* **562**, L167–L171 (2001).
19. Ellison, D. C., Slane, P. & Gaensler, B. M. Broad-band observations and modeling of the shell-type supernova remnant G347.3–0.5. *Astrophys. J.* **563**, 191–201 (2001).

20. Hartman, R. C. *et al.* The third EGRET catalog of high-energy gamma-ray sources. *Astrophys. J. Suppl.* **123**, 79–202 (1999).
21. Rybicki, G. B. & Lightman, A. P. *Radiation Processes in Astrophysics* (Wiley and Sons, New York, 1979).
22. Mathis, J. S., Mezger, P. J. & Panagia, N. Interstellar radiation field and dust temperatures in the diffuse interstellar matter and in giant molecular clouds. *Astron. Astrophys.* **128**, 212–229 (1983).
23. Walsh, A. J., Hyland, A. R., Robinson, G. & Burton, M. G. Studies of ultracompact HII regions—I. Methanol maser survey of IRAS-selected sources. *Mon. Not. R. Astron. Soc.* **291**, 261–278 (1997).
24. Aharonian, F. A., Atoyan, A. M. & Kifune, T. Inverse Compton gamma radiation of faint synchrotron X-ray nebulae around pulsars. *Mon. Not. R. Astron. Soc.* **291**, 162–176 (1997).
25. Sikora, M., Begelman, M. C. & Rees, M. J. Comptonization of diffuse ambient radiation by a relativistic jet: The source of gamma rays from blazars. *Astrophys. J.* **421**, 153–162 (1994).
26. Enomoto, R. *et al.* Design study of CANGAROO-III, stereoscopic imaging atmospheric Cherenkov telescopes for sub-TeV gamma-ray detection. *Astropart. Phys.* **16**, 234–244 (2002).
27. Enomoto, R., *et al.* in *Proc. 27th Int. Cosmic Ray Conf. (Hamburg)* (eds Simon, M., Lorenz, E. & Pohl, M.) Vol. 6, 2477–2480 (Copernicus Gesellschaft e.V., Katlenburg-Lindau, Germany, 2001).
28. Aharonian, F. A. *et al.* The energy spectrum of TeV gamma rays from the Crab nebula as measured by the HEGRA system of imaging air Cerenkov telescopes. *Astrophys. J.* **539**, 317–324 (2000).
29. Ishizaki, Y. *Spectra and Large-scale Isotropy of the Cosmic X-ray Background from ASCA observations* Thesis (Univ. Tokyo).

Acknowledgements

We thank H. Tomida for help in understanding the ASCA observational results, M. Seta for comments on molecular cloud density, and F. Aharonian for suggestions. This work was supported by a Grant-in-Aid for Scientific Research by the Japan Ministry of Education, Science, Sports and Culture, and the Australian Research Council.

Competing interests statement

The authors declare that they have no competing financial interests.

Correspondence and requests for materials should be addressed to R.E. (e-mail: enomoto@icrr.u-tokyo.ac.jp).

Atomic-scale imaging of individual dopant atoms and clusters in highly *n*-type bulk Si

P. M. Voyles*, D. A. Muller*, J. L. Grazul*, P. H. Citrin* & H.-J. L. Gossmann†

* Bell Laboratories, Lucent Technologies; and † Agere Systems, 700 Mountain Avenue, Murray Hill, New Jersey 07974, USA

As silicon-based transistors in integrated circuits grow smaller, the concentration of charge carriers generated by the introduction of impurity dopant atoms must steadily increase. Current technology, however, is rapidly approaching the limit at which introducing additional dopant atoms ceases to generate additional charge carriers because the dopants form electrically inactive clusters¹. Using annular dark-field scanning transmission electron microscopy, we report the direct, atomic-resolution observation of individual antimony (Sb) dopant atoms in crystalline Si, and identify the Sb clusters responsible for the saturation of charge carriers. The size, structure, and distribution of these clusters are determined with a Sb-atom detection efficiency of almost 100%. Although single heavy atoms on surfaces or supporting films have been visualized previously^{2–4}, our technique permits the imaging of individual dopants and clusters as they exist within actual devices.

Future generations of Si technology^{5,6} require free-electron densities in excess of 10^{21} electrons cm^{-3} . In some cases, this corresponds to concentrations of dopant atoms more than two orders of magnitude greater than their solid-solubility limit. Metastable growth techniques have significantly extended dopant concentrations beyond this limit, but the associated free-electron densities

are still found to be no higher than $\sim 5 \times 10^{20}$ electrons cm^{-3} (ref. 7). (Confining the dopants to a two-dimensional layer may help to sidestep this restriction in cases where very high-temperature processing is not required⁸.) It is therefore important to understand just how the dopant atoms become electrically inactive, leading to the observed saturation of free-electron densities.

Two generic models for electrically deactivating defect structures have been proposed for group V dopants in Si (that is, electron donors). The first model consists of between one and four dopant donor atoms surrounding a Si vacancy^{9–14}, and the second consists of only two donor atoms bound to reconfigured Si with no vacancies¹⁵. Determining which type of deactivating defect is formed in Si will establish how the fundamental limits to the free-electron concentration are reached.

We have used annular dark-field scanning transmission electron microscopy (ADF-STEM) to study highly Sb-doped Si. The samples were prepared by low-temperature molecular beam epitaxy, which provides high concentrations of Sb without introducing large amounts of Sb precipitates or Si vacancies¹⁶. The Sb density in the samples is 9.35×10^{20} atoms cm^{-3} , measured by Rutherford backscattering. The free-electron density from Hall measurements is 6.5×10^{20} electrons cm^{-3} , indicating that $\sim 30\%$ of the dopants are electrically inactive.

The STEM used here is state-of-the-art and has been optimized for very high stability during imaging¹⁷, but the real key to observing individual Sb atoms lies in the cross-section sample preparation. Simulations show that for a Si column containing a single Sb atom to be more than 25% brighter than a pure Si column, the sample must be less than 50 Å thick. Random variations in thickness must be less than the contrast of one Sb atom, and the surfaces must be free from native amorphous SiO₂ layers and damaged bulk Si layers amorphized during thinning. These rigorous requirements are achieved using chemical-mechanical polishing techniques and an etch to remove the surface oxide as described in the Methods section. We do not use ion milling due to the unavoidable damage from implantation that could be mistaken for dopant clusters.

Figure 1 is an ADF-STEM image of a cross-section of the sample in the (110) zone-axis orientation. The brightest dots on the left are atomic columns containing at least one Sb atom. The undoped region on the right shows no such very bright dots. Two images,

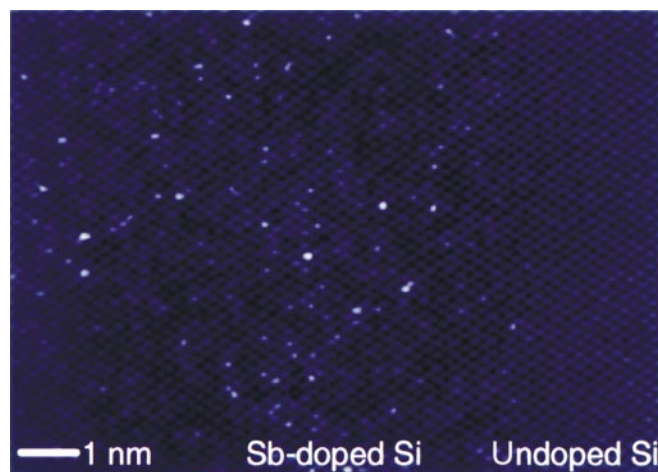


Figure 1 Annular dark-field scanning transmission electron microscopy image of a cross-section of highly Sb-doped Si. The brightest dots (left) are atomic columns containing one or more Sb atoms, absent in substrate (right), where there is no Sb. Thickness variations along the wedge have been subtracted using a second-order polynomial fit. The image has been low-pass filtered to remove scan noise, and is displayed with a nonlinear intensity scale to highlight bright features.